

## NUMERICAL EXPLORATION OF LOW ALTITUDE ROCKET PLUME IN AIRCRAFT VICINITY

Malsur Dharavath; P. Manna; Debasis Chakraborty  
 Directorate of Computational Dynamics  
 Defence Research and Development Laboratory (DRDL)  
 Kanchanbagh Post, Hyderabad-500 058  
 Email : debasis\_cfd@drdl.drdo.in; debasis\_drld@yahoo.co.in

### Abstract

*Low altitude plume of a solid rocket motor is numerically explored. The effects of free stream Mach number, altitude and presence of launch platform wing on plume shape are studied. Three-dimensional Reynolds Averaged Navier-Stokes (RANS) equations along with k- $\epsilon$  turbulence model and species transport equations are solved using commercial CFD software CFX-11. Thermochemical parameters (Mach number, pressure, temperature and propellant hot gas mass fraction) are analysed to characterize the plume. Mixing layer boundaries, its thickness and the attainment of self-similarity are evaluated to study the plume structure. With the increase of free stream Mach number, the computed plume diameter reduces. Centerline pressure, temperature and radial expansion of the plumes increases with the increase in altitude. Plume is found to be elongated and narrowed with relatively warm core region due to the presence of platform wing.*

### Introduction

Rocket Engine plumes are high energy multi-component flow field coming out from a rocket nozzle expanding into the surrounding environment. The prediction of plume properties such as temperature, velocity, pressure, chemical species concentrations and turbulence properties is a formidable task for many aerospace design problems. The design of jet deflector of launch vehicles and missiles, missile separation from fighter aircraft/helicopter, plume ducting system for canisterized missiles, jettisoning of spent stages of multistage rockets, plume impingement on satellite and other spacecraft at higher altitude etc. requires accurate prediction of plume characteristics. Understandings of the finer details of plume structure are important for both fundamental fluid mechanics studies and practical applications. The problem continues to be research subject in present days.

Characterization of rocket exhaust plume is explained in the literature [1,2] which is dominated by turbulent mixing, afterburning and strong wave process. The schematic of low altitude plume with supersonic free stream is shown in Fig.1. The flow at the nozzle exit undergoes Prandtl-Meyer expansion and accelerates. It contains a

complex periodic shock cell structure created by the imbalance of static pressure between the plume core and ambient. The plume equilibrates to atmospheric pressure through a repetitive series of waves which decay due to shock, turbulence and particle induced viscous dissipation. The mixing and after burning process initiate at the shear layer which demarcate the hot rocket exhaust and external flow. Underexpanded plumes in a supersonic co-flowing stream are different from those issuing into a quiescent gas. The atmospheric pressure boundary redirects the discrete expansion waves towards the plume centerline as a series of compression waves, which coalesces to form oblique intersecting incident shock. This barrel like shock separating the inner jet core from the outer sheath of supersonic fluid terminates at the Mach disk. These shock structures finally break down to fully turbulent stream due to the compressible shear layer at the outer edge of the jet. The plume structure can be divided into three regions: near field, transition region and far field. In the near field, the nozzle exhausts dominates the complete plume structure. In the transition region, mixing of the hot gases with the atmosphere takes place at the boundary and in the far field, the core flow diminishes and the mixing with the ambient environment takes full effect. For high altitude plumes, Moran [3] defined the plume

scale as  $L = \sqrt{N} D$  ( $N$  and  $D$  are the pressure ratio and nozzle throat diameter respectively). It was not immediately obvious that for a low altitude plume with complex interaction between the rocket body, its boundary layers, the plume and the freestream, whether there exists a simple plume scale that could normalise plume and barrel shock positions to a common structure.

Underexpanded free jet flow field was investigated by theoretical, experimental, and numerical methods. Englert [4] used series solution to provide an operational method for determining the initial contour and pressure field about a supersonic jet. Earlier studies [5,6] concentrated on measurement of shock cell size and Mach disk location to characterize the underexpanded jets. Love et al. [5] studied the underexpanded plume in quiescent atmosphere both experimentally and theoretically and analysed various plume parameters like Mach disk size and location and primary wave length etc. Adamson and Nicholls [6] used Method of Characteristics (MOC) to calculate the centerline Mach number distribution and Mach disk location as a function of stagnation pressure over a range of flow conditions in both sonic and supersonic underexpanded jets. Tannehill and Anderson [7] have extended Lagrangian finite-difference technique developed for calculating the flow in high-altitude rocket exhaust plumes to intermediate-altitude rocket exhaust plumes by incorporating chemical nonequilibrium and turbulent transport capabilities into the boundary layer analysis.

Measurements in supersonic plumes are difficult because of non-suitability of direct measurement method, due to varying static pressure, high velocities and shocks. Nonintrusive flow measurement techniques, namely laser doppler anemometry and laser induced fluorescence are employed to measure various flow parameters in the underexpanded plumes [8-9]. Moris et al. [2] provided important experimental plume parameters data in low altitude (~30 km.) in hypersonic Mach number (~7) with the help of schlieren photographs and pressure measurements. Eckroth et al. [10] measured heat flux rates, pressures, and temperatures on jet deflector of space shuttle and shown that design specification overpredicts heating rates by a factor of three and underpredicts pressures by a factor of two. Centreline rocket plume temperature distribution were measured [11] to study the heat transfer analysis of launch carriers. Reliable measurement of velocity and turbulent quantities of the low altitude plume is

still very limited for the validation of computational model.

CFD techniques are matured and playing an increasingly important role in aerospace designs and in exploring the complex flow physics. While applying a computational tool in engineering application, validation and checking its range of application is of vital interest. Various Euler [13] and Parabolised Navier Stokes (PNS) [2,13-14] methods are employed in the simulation of underexpanded jet and the methods overpredict the shock structure and underpredict the mixing rate. Navier-Stokes calculations [15-16] with  $k-\epsilon$  turbulence model showed promising results to capture the underexpanded jet flow structure. Birkby and Page [17] used Navier-Stokes equations and  $k-\epsilon$  turbulence model with compressibility corrections to simulate underexpanded jet flow field using a pressure based methodology. Their simulations predict correct shock-cell wavelength but decay was too rapid compared to the experimental results. J. Sahu [18] employed a thin-layer compressible Navier-Stokes code to compute supersonic flow over an axisymmetric missile after body containing a centered exhaust jet with exit Mach number of 2.5. Candler et al. [19] studied Atlas-II motor plume with the help of third order accurate upwind finite volume solver. Gussmann et al. [20] used the CFD code OVERFLOW [21] to rocket plume of High Lift Launch Vehicle (HLLV) and compared the computed plume profiles with flight observations. Chakraborty et al. [22] and Malsur et al. [23] studied the base flow structure in supersonic free stream in the presence of nozzle plume. Specialized computer models have been developed [24] to predict rocket plume with multiphase flow effects modelled through Lagrangian and Eulerian reference. Several state-of-the-art computer codes (PARCH, CRAFT, and SCHAFT) [16,25] are employed to study missile exhaust plume. These codes have been extended to include advanced turbulence models, generalized thermochemistry, and multiphase nonequilibrium models. Recently, Gonzalez et al. [26] used commercial CFD solver Ansys Fluent [27] to study near field plume behavior to assess the standoff distance from the launch platform for a store with a small solid rocket motor.

In the present work, thermochemical characteristics of a solid rocket motor plume launched from an airborne platform is numerically simulated. Three dimensional Reynolds Averaged Navier Stokes (RANS) equations are solved along with two equation turbulence models using

a commercial CFD software. The effect of altitude, free stream Mach number and aircraft wing on plume characteristics is studied parametrically.

### Geometry and Mesh Generation

In the present study, isolated missile without the presence of aircraft as well as the missile with the presence of aircraft is considered for numerical simulations. Isolated missile without the presence of the aircraft is considered as baseline configuration (Case-1) which is shown in Fig.2. Since, the missile is an axi-symmetric geometry (ignoring the effect of fins), a  $10^\circ$  sector is considered for computational domain (shown in Fig.3) to reduce the computational time. Origin of the domain is taken on the axis of the missile exit plane. For the simulation, X-axis is considered along the flow direction, while Y-axis and Z-axis are taken in the vertical and side direction respectively. The domain is considered sufficiently large to capture all the flow phenomena. It is extended 42D in radial direction and 318 D in downstream of missile base along the flow direction, where, D represents nozzle exit diameter. Multi-block structured grid with total elements of 0.42 million ( $618 \times 85 \times 8$  in longitudinal, radial and azimuthal directions respectively) for  $10^\circ$  sector geometry are generated using ICEM-CFD grid generator [28]. Typical grid distribution on the symmetry plane ( $Z = 0.0$  m) with zoomed view of nozzle region is shown in Fig.4. The grids are very fine ( $Y^+ \sim 1.0$ ) at nozzle, missile walls, and core flow regions. Nozzle inlet boundary conditions along with propellant gas properties are given in Table-1.

### Computational Methodology

Commercial CFD software, CFX-11 [29] is used for the simulation. It solves 3-D Reynolds Averaged Navier Stokes (RANS) equations on structured/unstructured grid

Table-1 : Inflow Boundary Conditions		
Property	Propellant Gas	Free-Stream
$P_0/P_\infty$	216.6	1.276
$T_0/T_\infty$	10.5	1.072
Molecular weight (kg/kmol)	24.5	28.9
$C_p$ (J/kg K)	2336	1004
Dynamic Viscosity (Pa - sec)	8.55e-05	1.63e-05
Thermal conductivity (W/m K)	0.3822	0.02426

and is based on finite volume approach. It solves various turbulence models viz.  $k-\epsilon$ ,  $k-\omega$  or  $SST$  turbulence model etc. along with RANS equations. The software has three major modules, (i) preprocessor - imports grid from ICEM-CFD as a grid generator and sets up the boundary condition, initial field condition and turbulence models (ii) solver manager - solves the flow field based on the grid and the boundary condition and (iii) postprocessor - helps in analyzing and visualizing flow field data.

It utilizes high resolution numerical schemes to ensure global convergence of mass, momentum, energy and species. In the present study, the discretization of the convective terms is done by the second order difference scheme. Local time stepping has been used to obtain steady-state solutions. The  $k-\epsilon$  turbulence model is used along with standard wall function.

### Governing Equations

The appropriate system of equations governing the turbulent compressible flow is written as:

Conservation of mass:

$$\frac{\partial \rho}{\partial t} + \frac{\partial}{\partial x_i} (\rho u_i) = 0 \quad i = 1, 2, 3$$

Conservation of momentum:

$$\frac{\partial}{\partial t} (\rho u_i) + \frac{\partial}{\partial x_j} (\rho u_i u_j) + \frac{\partial p}{\partial x_i} = \frac{\partial \tau_{ij}}{\partial x_j}, \quad i, j = 1, 2, 3$$

Conservation of energy:

$$\frac{\partial}{\partial t} (\rho H) + \frac{\partial}{\partial x_i} (\rho u_i H) = - \frac{\partial}{\partial x_i} (u_i \tau_{ij}) + \frac{\partial q_i}{\partial x_i}$$

Conservation of species mass fraction:

$$\frac{\partial}{\partial t} (\rho Y_n) + \frac{\partial}{\partial x_i} (\rho Y_n u_i) = \frac{\partial}{\partial x_i} (-\vec{J}_i) + \dot{\omega}_n \quad i = 1, 2, 3$$

Where,  $\rho$ ,  $u_i$ ,  $p$ ,  $H$ ,  $Y_n$ ,  $\tau_{ij}$ ,  $q_i$ ,  $J_i$  and  $\dot{\omega}_n$  are the density, velocity components, pressure, total energy, mass fraction for species  $n$ , laminar viscous stress tensor, heat flux vector, diffusion mass flux and chemical source term for species  $n$  respectively. To complete the aforementioned governing equations, the following closure relations are

needed. The diffusion mass flux  $\vec{J}_i$  (the relative mass flux) in turbulent flows can be written as:

$$\vec{J}_i = \left( \rho D_{i,n} + \frac{\mu_t}{Sc_t} \right) \frac{\partial Y_n}{\partial x}$$

Where,  $D_{i,n}$  is laminar diffusivity and  $Sc_t$  is turbulent Schmidt number which is given by,

$$Sc_t = \frac{\mu_t}{\rho D_t}$$

Where,  $\mu_t$  is turbulent viscosity and  $D_t$  is turbulent diffusivity.  $Sc_t$  is a measure of the relative importance of momentum transfer to mass transfer and a value of 0.7 is used for the present work. The laminar viscous stress tensor is given by,

$$\tau_{ij} = \mu \left[ \frac{\partial u_i}{\partial x_j} + \frac{\partial u_j}{\partial x_i} \right] - \frac{2}{3} \delta_{ij} \mu \frac{\partial u_k}{\partial x_k}$$

The multi-species heat flux vector can be written as the sum of Fourier's Law for heat conduction and the heat flux due to diffusion produced by concentration gradients:

$$q_i = -K_{eff} \frac{\partial T}{\partial x_i} + \rho \sum_{n=1}^{NS} h_n Y_n u_{n,i}$$

Where,  $K_{eff}$  is effective thermal conductivity (sum of laminar and turbulent parts of thermal conductivity in the gaseous medium).

### k-ε Turbulence Model

The simplest complete models of turbulence are two equation models in which the solution of two separate transport equations allows the turbulent velocity and length scales to be independently determined. The turbulent viscosity is calculated as function of  $k$  and  $\epsilon$  as proposed by Spalding [30] and is given below:

$$\mu_t = \rho C_\mu \frac{k^2}{\epsilon}$$

Turbulent kinetic energy ( $k$ ) equation:

$$\frac{\partial}{\partial t} (\rho k) + \frac{\partial}{\partial x_i} (\rho k u_i) = \frac{\partial}{\partial x_j} \left[ \left( \mu + \frac{\mu_t}{\sigma_k} \right) \frac{\partial k}{\partial x_j} \right] + G_k - \rho \epsilon - Y_M$$

Rate of dissipation of turbulent kinetic energy ( $\epsilon$ ) equation:

$$\frac{\partial}{\partial t} (\rho \epsilon) + \frac{\partial}{\partial x_i} (\rho \epsilon u_i) = \frac{\partial}{\partial x_j} \left[ \left( \mu + \frac{\mu_t}{\sigma_\epsilon} \right) \frac{\partial \epsilon}{\partial x_j} \right] + G_\epsilon C_{1\epsilon} \frac{\epsilon}{k} - C_{2\epsilon} \rho \frac{\epsilon^2}{k}$$

The model constants are taken as,  $C_{1\epsilon} = 1.44$ ,  $C_{2\epsilon} = 1.92$ ,  $C_\mu = 0.09$ ,  $\sigma_k = 1.0$ ,  $\sigma_\epsilon = 1.3$ , where,  $G_k$  is the generation of turbulence kinetic energy due to the mean velocity gradients, calculated as  $G_k = -\rho \overline{u'_i u'_j} \frac{\partial u_j}{\partial x_i}$  and  $Y_M$  represents compressibility effects given by,  $Y_M = 2 \rho \epsilon M_t^2$ .

The turbulent Mach number  $M_t$  is given by  $M_t = \sqrt{\frac{k}{a^2}}$ .

To find out the accuracy and the range of applications, the software has been validated for various complex aerospace problems including supersonic base flow [23], free stream and rocket exhaust interaction [31], transverse sonic injection in supersonic stream [32], supersonic jet impingement problem in an inclined plate [33], missile movement in canister [34] etc. and obtained very good match with experimental and flight measured values.

## Results and Discussions

### Boundary Conditions

Numerical simulations are carried out to study plume characteristics of the missile with / without the presence of aircraft for zero Angle-of-Attack (AOA) at 5 km altitude with two different free stream Mach numbers ( $M_\infty$ ) 0.6 and 0.8. Computational domain with boundary conditions is provided in Fig.3. Propellant gas properties and free stream inflow conditions at 5 km altitude (taken from Indian standard atmospheric model) are provided in Table-1. No-slip and adiabatic boundary conditions are imposed at nozzle walls and missile body. Maximum residual ( $= \phi_j^{n+1} - f(\phi_j^{n+1}, \phi_j^n)$ )  $< 10^{-4}$  and domain mass imbalance 0.1% is considered as convergence criteria.

### Base Line Results: Missile Speed ( $M_\infty$ ) of 0.6 and Altitude = 5 km

Jet is moderately under-expanded with nozzle exit pressure ratio (nozzle exit static pressure ( $P_j$ ) to free-stream static pressure ( $P_\infty$ )) of 2.4. The occurrence of the

shock in the jet due to interaction of propellant hot gas exhaust and free stream is crisply captured as seen from symmetry plane Mach number contour in Fig.5. The zoomed view of the contour near missile base is also presented. The hot propellant gas underexpands, and the pressure of the ambient gas at the boundary acts like a piston and pushes the jet gas back towards the axis, creating pressure and temperature to rise. When the incident shock reaches at the axis of the jet, it undergoes a regular reflection; that is, it forms a diverging shock. At the point where this reflected shock reaches the jet boundary, it knocks the boundary outward, creating a new expansion fan, and the process begins all over again. This pattern of shock waves zones is repeated several times in the core of the plume, while the strength of the shock and the rise in temperature or pressure are reduced in each time which is dependent on nozzle exit to free stream pressure ratio.

Axial distribution of Mach number and static pressure along the plume centerline is shown in Figs.6(a) to (b) respectively. Adjacent to the nozzle exit, both Mach number and static pressure show up and down pattern due to the presence of various shock structures as explained earlier. Beyond  $X/D \sim 12$ , Mach number decreases gradually due to the divergence of the hot gas plume and mixing with ambient air. Core Mach number becomes fully subsonic at about  $X/D=40.0$ . Two pressure peaks are seen in the locations where the incident shocks meet the axis. The radial distributions of pressure ratios at various axial locations [ $X/D = 7.94, 15.87, 23.81$  and  $31.74$ ] are presented in Fig.7 which decrease gradually from the core towards the farfield to attain free stream value. Local static pressure becomes equal to the free stream static pressure in the core of the plume at an axial distance of  $X/D= 23.7$ . Static temperature and propellant hot gas mass fraction distribution on symmetry plane are shown in Figs.8(a) and (b) respectively. Both static temperature and hot propellant gas mass fraction are reduced due to mixing with ambient air as we move downstream but the core remains sufficiently hot for long distance ( $\sim X/D = 178$ ) in the downstream from the nozzle exit.

At the nozzle base region static temperature begins to fall due to the expansion of the flow, but increases suddenly when the incidence shocks impinge on the axis. Then again it decreases due to the 2<sup>nd</sup> expansion of the flow and increases again when the incidence shocks meet at the axis. The static temperature sharply falls beyond  $X/D \sim 20.0$  to 100. Centerline of the plume remains hotter for long distance and  $T/T_\infty$  is of the order of 1.25 at computational domain exit ( $X/D \sim 318$ ). Maximum tem-

perature is found to occur always at the centerline for a particular axial location as seen from static temperature radial distribution at different axial stations presented in Fig.9. The maximum plume diameter ( $D_p$ ) is found to be  $32D$  at  $X/D = 318$ . The plume diameter is defined as the boundary where local static temperature is  $T/T_\infty = 1.01$  (1% more than the free stream air). Comparing the pressure and temperature profiles, we can conclude that while the plume pressure equalizes with the atmospheric pressure at a very short distance; temperature profiles shows deviation from the atmospheric values upto a large distance.

The mixing layer boundaries ( $\delta_{0.0}, \delta_{0.99}$ ) are calculated corresponding to the mass fraction of propellant hot gas 0.01 and 0.99 and the thickness of the mixing layer between the nozzle jet and free stream flow is defined as  $\nabla\delta = (\delta_{0.01} - \delta_{0.99})$  which are shown in Figs.10(a) and (b) respectively. Core regions of the plume remain almost propellant gas rich (more than 99%) upto  $X/D = 9.0$  and the mixing-layer growth rate is 0.06547. The nondimensionalised velocity profiles ( $u/u_{noz\ exit}$ ) [ $u_{noz\ exit}$  is free stream central jet velocity] at various axial locations,  $X/D= 40, 79, 119, 159, 198, 238$  and  $317$  are plotted against nondimensionalised distance ( $Y/\nabla\delta$ ) in Fig.11. We can observe that the velocity profile has collapsed into single curve indicating the attainment of self similarity at  $X/D = 79$ .

### Effect of Free Stream Mach Number ( $M_\infty$ ) on Plume Shape

Numerical simulations are carried out to study plume characteristics at higher free stream Mach number ( $M_\infty \sim 0.8$ ) while keeping all other boundary conditions same as mentioned in Table-1. The Mach number and static temperature distributions at plume centerline for these cases are almost identical as shown in Fig.12. However, core Mach number is found slightly more in the downstream direction for  $M_\infty=0.8$  condition.

The comparison of temperature profiles at three different axial locations ( $X/D = 80, 160$  and  $320$ ) for two free stream Mach numbers are compared in Figs.13(a) to (c). It is observed that, for a particular axial location, static temperature profile slightly reduced for higher missile speed ( $M_\infty = 0.8$ ) and the plume is compressed. The computed maximum plume diameter is  $28.7D$  for  $M_\infty=0.8$  against  $31D$  for  $M_\infty = 0.6$ .

### Effect of Altitude on the Plume Shape

In addition to the base line case ( $H=5$  km), two more simulations are carried out for altitude of 1 km and 10 km for  $M_\infty=0.6$  to study the plume characteristics at three different altitudes. The jet pressure ratios for the three altitudes (1 km, 5 km and 10 km) are 1.88, 3.01 and 5.91 respectively. From static pressure profile comparison at different axial locations for three altitudes cases (Fig.14), it is observed that, with the increase in altitude, both the centerline pressure and radial expansion increases. The more radial expansion of the plume at higher altitude is due to lesser compression of surrounding air. The center line static pressure becomes equal to free stream pressure within  $X/D$  of 32. The temperature profiles at three different altitudes are shown in Fig.15. The effect of altitude on temperature profile is more predominant than pressure. Temperatures are higher and profiles are broader for higher altitude plumes.

### Effect of Platform Wing on Plume Shape

The schematic of the mounting of the aerospace vehicle on air borne platform along with the computational domain is presented in Fig.16. To estimate the effect of wing of the platform on the plume, truncated geometry of the wing is considered and a new simulation is carried out considering full 360 degree sector. The domain is extended by  $14D$  in front of missile nose and by  $160D$  downstream of missile base along the axial direction. Top and bottom boundaries are placed at  $21D$  and  $15D$  respectively from the missile axis. Side boundaries are located at  $11D$  apart from the missile axis. Hybrid grids (combination of structure and unstructured grid) are generated with a total number of elements of 5.7 million for the aerospace vehicle along with the platform wing. The mixing of hot rocket exhaust with free stream air is considered by taking air and hot exhaust as two different species and solving separate transport equations for them. Although in some cases, unburnt species present in plumes react with ambient air, for the current propellant composition (smokeless), it is assumed that reaction is complete within the rocket nozzle itself. Hence, no reaction with free stream air is modeled. The simulation results with and without platform wing are compared.

The Mach number distribution around the missile near the wing is compared with Mach number for isolated case in Fig.17. The plume in the former case is seen to be elongated and narrow compared to the isolated one. Significant flow compression is observed near the wing vi-

city. Shock cell structure in the plume in the presence of wing is seen to be different than that of isolated plume in the vicinity of the rocket nozzle. The plume boundaries between the two cases are compared in Fig.18. The disturbance and compression of free stream due to the presence of the wing is mainly responsible for the narrowness and elongation of the plume. Comparison of static temperature ratio at various axial locations is shown in Fig.19. The temperature distribution is not the same on either side of the centerline in case of aircraft wing, though it is almost identical for isolated case. The core region is found to have more temperature in presence of aircraft wing compared to the isolated case. However, at larger  $X/D$  ( $\sim 120$ ), the temperature profiles between the two cases are the same.

### Conclusions

The effects of free stream Mach number, altitude and presence of launch platform wing on plume shape of a solid rocket motor are estimated through CFD analysis. 3-D RANS equations along with two equations  $k-\epsilon$  turbulence model and species (propellant gas and ideal air) transport equations are solved using commercial CFD software CFX-11. Details of the flow field including the missile center line properties like Mach number, pressure, temperature and propellant hot gas mass fraction are analysed to characterize the plume. Centerline properties are found to decrease at downstream of the missile base due to the mixing of the propellant hot gas with the free stream air. Self-similarity of velocity is found to be attained at  $X/D=79$ . The computed maximum plume diameter reduces marginally  $28.7D$  for  $M_\infty=0.8$  against  $31D$  for  $M_\infty=0.6$ . With the increase in altitude, the centerline pressure, temperature and radial expansion of the plumes increase. In the presence of platform wing, plume is found to be elongated, narrowed and irregular shape in the near field with relatively warm core region.

### References

1. Dash, S. M., Wolf, D. E., Beddini, R. A. and Pergament, H. S., "Analysis of Two-phase Flow Processes in Rocket Exhaust Plumes", Journal of Spacecrafts and Rockets, Vol.22, No.3, May-June 1985, pp.367-380.
2. Morris, N., Buttsworth, D., Jones, T. and Brescianini, C., "An Experimental and Computational Study of Moderately Underexpanded Rocket Exhaust Plumes in a Co-flowing Hypersonic Free Stream", AIAA-95-6127.

3. Moran, J.P., "Similarity in High Altitude Jets", AIAA Journal, Vol.5. No.7, 1967, pp.1343-1345.
4. Englert, G.W., "Operational Method of Determining initial Contour and Pressure Field About a Supersonic Jet", NASA TND 279, 1960.
5. Love, E.S., Grisby, C.E., Lee, L.P. and Woodling, M.J., "Experimental and Theoretical Studies of Axisymmetric Free Jets", NASA TR R-6, 1959, NASA.
6. Adamson, T.C. Jr. and Nicholls, J.A., "On the Structure of Jets From Highly Underexpanded Nozzles into Still Air", Journal of Aerospace Sciences, Vol.26, No.1, 1959, pp.16-24.
7. Tannehill, J. C. and Anderson, E. W., "Intermediate Altitude Rocket Exhaust Plumes", J. Spacecraft, Vol.8, No.10, 1973, pp.1052- 1057.
8. Chuech, S.G., Lai, M.C. and Faeth, G.M., "Structure of Turbulent Underexpanded Free Jets", AIAA Journal, Vol.27, 1989, pp.549-559.
9. Wilkes, J.A., Glass, C.E., Danchy, P.M. and Nowak, R. J., "Fluorescence Imaging of Underexpanded Jets and Comparison with CFD", AIAA Paper No. 2006-910, 2006.
10. Eckroth, W.V., Struchen, L., Thomas, T., Rafael, P., Nerolich Shaun and Parlier, C., "Space Shuttle Solid Rocket Motor Plume Pressure and Heat Rate Measurements", Journal of Spacecraft and Rockets, Vol.51, No.1, January-February 2014, pp.281-295.
11. Qiangfeng Huang., Xiong Wan., Zhimin Zhang., Huaming Zhang., Hengyang Shen and Tingting Du., "Based on Fluent Numerical Calculation of Refractive Index on Rocket Engine Nozzle Plume", Optics and Photonics Journal, No.3, 2013, pp.90-93.
12. Matsuda, T., Umedy, Y., Ishii, R., Yasuda, A. and Sawada, K., "Numerical and Experimental Studies on Choked Underexpanded Jets" AIAA Paper No. 87-1378, 1987.
13. Dash, S. M., Wolf, D.E. and Seiner, J.M., "Analysis of Turbulent Underexpanded Jets, Part 1: Parabolized Navier-Stokes Model, SCIPVS", AIAA Journal Vol.23, No.4, April 1985, pp.505-514.
14. Abdol-Hamid, K.S. and Wilmoth, R.G., "Multiscale Turbulence Effects in Underexpanded Supersonic Jet", AIAA Journal, Vol.27, 1989, pp.315-322.
15. Cumber, P.S., Fairweather, M., Falle, S.A.E.G. and Giddings, J.R., "Predictions of the Structure of Turbulent, Moderately Underexpanded Jets", Trans. ASME, Journal of Fluid Engineering, Vol.116, 1994, pp.703-713.
16. York, B. J., Sinha, N., Dash, S. M., Hosangadi, A., Kenzakowski, D. C. and Lee, R. A., "Complete Analysis of Steady and Transient Missile Aerodynamic/Propulsive/Plume Flowfield Interactions", AIAA 1992-3603.
17. Birkby, P. and Page, G.J., "Numerical Predictions of Turbulent Underexpanded Sonic Jets Using a Pressure-based Methodology", Proceedings of IME - Part G, Journal of Aerospace Engineering, Vol.215, No.3, 2001, pp.165-173.
18. Sahu, J., "Computations of Supersonic Flow Over a Missile Afterbody Containing an Exhaust Jet", Journal of Spacecraft and Rockets, Vol.24, No.5, September-October 1987, pp.403-410.
19. Candler, G. V., Rao, R. M., Sinha, K. and Levin, D. A., "Numerical Simulations of Atlas-II Rocket Motor Plumes", AIAA Paper No.2001-0354.
20. Marshall Gusman., Jeffrey Housman and Cetin Kiris., "Best Practices for CFD Simulations of Launch Vehicle Ascent with Plumes - Overflow Perspective", 49<sup>th</sup> AIAA Aerospace Sciences Meeting, January, 4-7, 2011, Orlando, FL, pp.1-15.
21. Nichols, R. and Buning, P., Users Manual for Overflow 2.1, Version 2.1t.
22. Chakraborty, D. Kumar, P., Balu, R. and Adimurthy, V., "Numerical Simulation of Axisymmetric Base Flow in the Presence of Propulsive Jet", Journal of Aeronautical Society of India, Vol.53, No.1, Feb/Mar 2001, pp.35-38.
23. Malsur Dharavath, Sinha, P. K. and Debasis Chakraborty., "Simulation of Supersonic Base Flow Effect of Computational Grid and Turbulence Model", ASME Journal of Aerospace Engineering, Vol.224, No.3, 2010, pp.311-319.

24. Federico Montanari., Fritz Bedford., John F. Widmann and Konstantin A. Kurbatskii., "Multiphase CFD Analysis of Solid Rocket Motor Nozzle and Plume Flow", AIAA 2007-923.

25. York, B. J., Sinha, N., Dash, S. M., Anderson, L. and Gominho, L., "Navier-Stokes Simulation of Plume/Vertical Launching System Interaction Flow-Fields", AIAA 1992-0839.

26. González D. R., Wallman, P., Sanford M., Monat, J. and Joel, C., "Characterization of Rocket-Plume Fluid-Dynamic Environment using Numerical and Experimental Approaches", Journal of Spacecraft and Rockets, Vol.50, No.3, May-June 2013, pp.527-539.

27. ANSYS FLUENT, Software Package, Ver.12.1, ANSYS, Inc., Canonsburg, PA, 2010.

28. ANSYS ICEM-CFD-11, Installation and overview, January, 2007.

29. ANSYS CFX-11, Installation and overview, January, 2007.

30. Launder, B.E. and Spalding, D.B., "The Numerical Computation of Turbulent Flows", Computational Methods Applied Mechanical Engineering, Vol.3, 1974, pp.269-289.

31. Saha, S., Rathod, S., Chandra Murty, M. S. R., Sinha, P. K. and Debasis Chakraborty., "Numerical Simulation of Base Flow of a Long Range Flight Vehicle", ActaAstronautica, Vol.74, No.3, May-June 2012, pp.112-119.

32. Aswin, G. and Debasis Chakraborty., "Numerical Simulation of Transverse Side Jet Interaction with Supersonic Free Stream", Aerospace Sciences and Technologies Journal, Vol.14, 2010, pp.295-301.

33. Malsur Dharavath and Debasis Chakraborty., "Numerical Simulation of Supersonic Jet Impingement on Inclined Plate", Defense Science Journal, Vol.63, N0.4, July 2013, pp.355-362.

34. Sinha, P. K. and Debasis Chakraborty., "Numerical Study of Flow Inside a Tube During Hot Launching of Rocket", Journal of Aerospace Engineering, Vol.228, December 2014, pp.2604-2611.

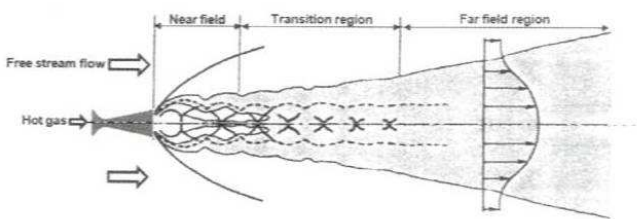


Fig.1 Schematic Picture of the Plume Structure

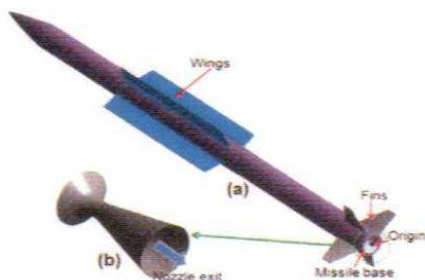


Fig.2 Schematic of (a) Isolated Aerospace Vehicle (b) Nozzle

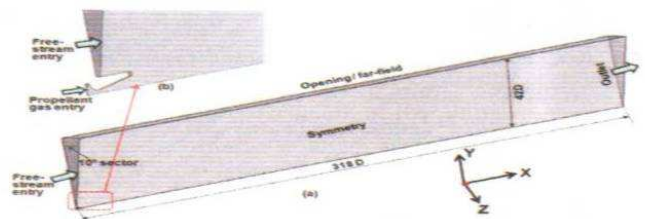


Fig.3 Schematic of (a) Computational Domain with 10° Sector and (b) Zoomed View Near Nozzle

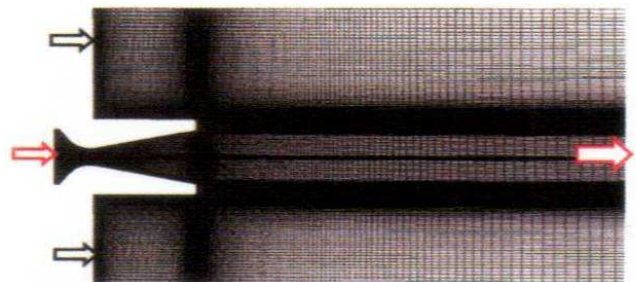


Fig.4 Typical Grid Distribution at the Near Field of Nozzle Region



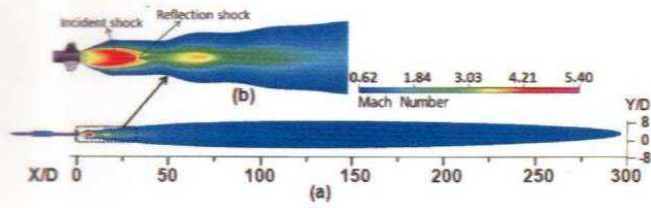


Fig. 5 Contour of Mach Number Distribution, (a) Symmetry Plane (i.e.  $Z = 0.0$  m) and (b) Exploded View at Vehicle Base

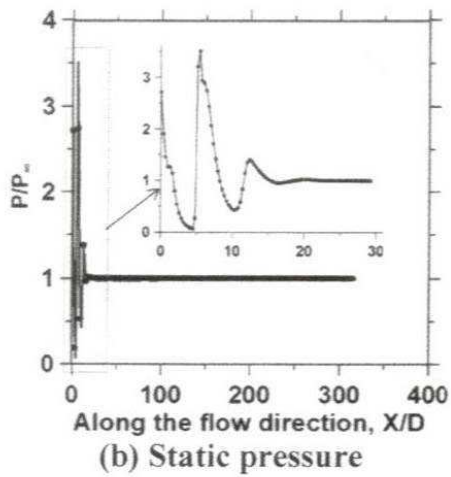
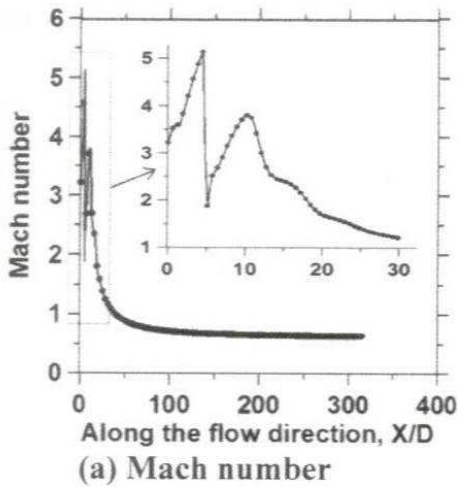


Fig. 6 Various Centerline Properties Along the Flow Direction from Missile Base

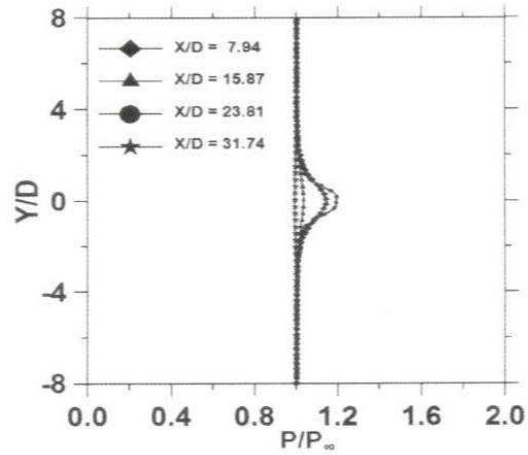


Fig. 7 Static Pressure Profiles Along the Radial Direction at Four Different Axial Locations

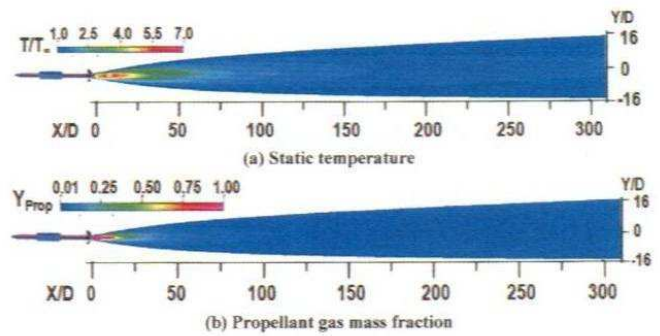


Fig. 8 Various Contour Distribution on Symmetry Plane Near Missile Base Region

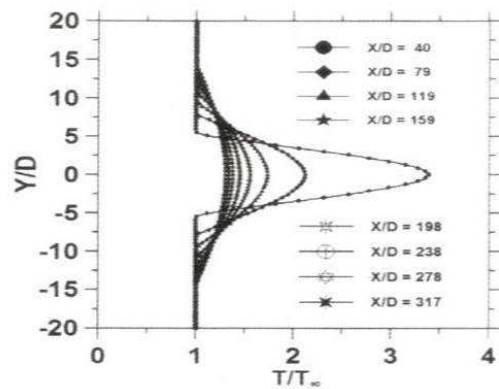


Fig. 9 Static Temperature Profiles Along the Radial Direction at Various Axial Locations

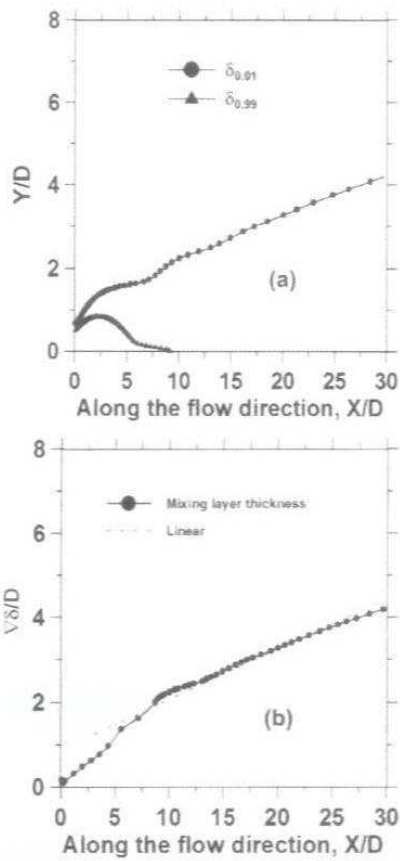


Fig.10 (a) Computed Plume Shape (b) Mixing Layer Thickness

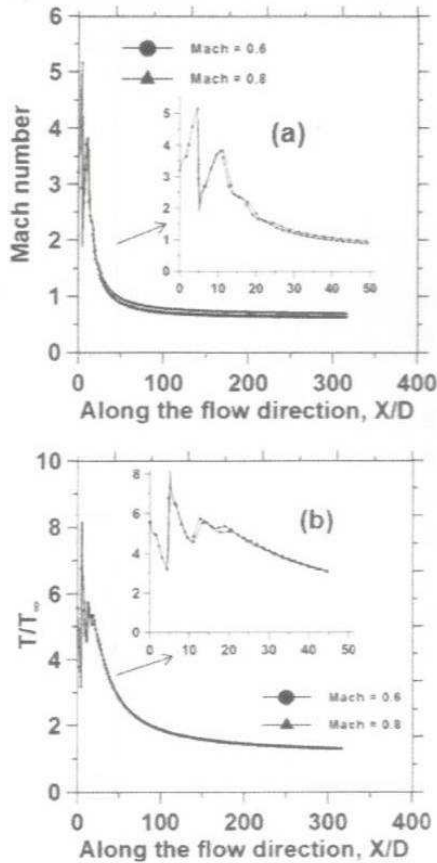


Fig.12 Comparison of Centerline Properties of Missile at Two Different Missile Speed, (a) Mach Number and (b) Static Temperature Ratio

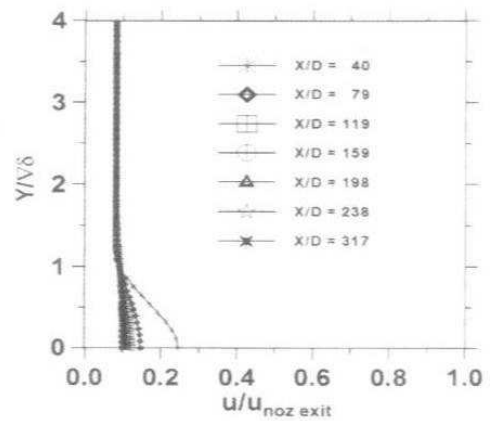


Fig.11 Non-dimensionalised Velocity Profile at Various Axial Locations

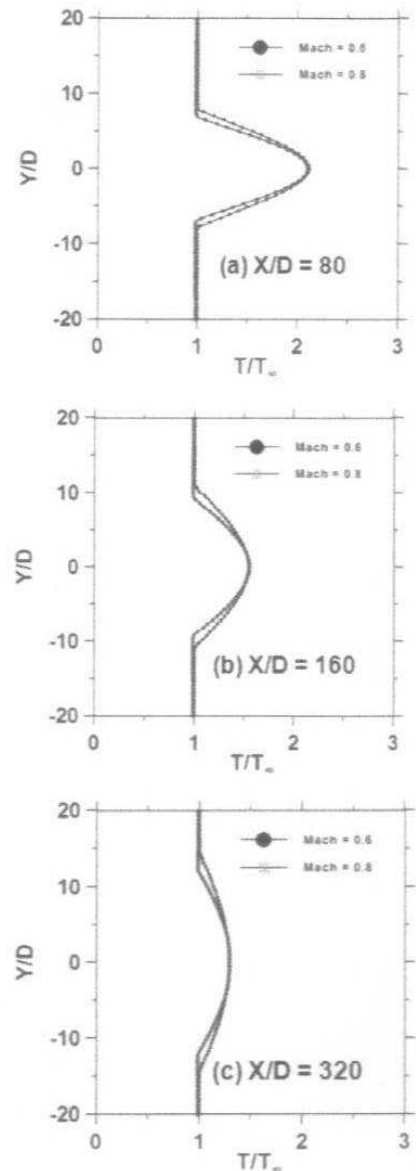


Fig.13 Comparison of Temperature Profiles at Three Different Axial Locations

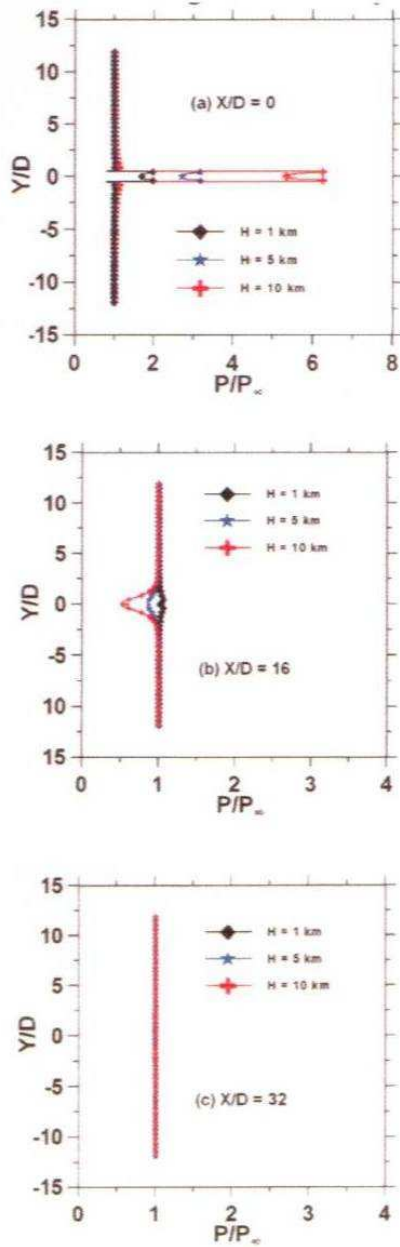


Fig.14 Comparison of Static Pressure Profiles at Different Axial Locations

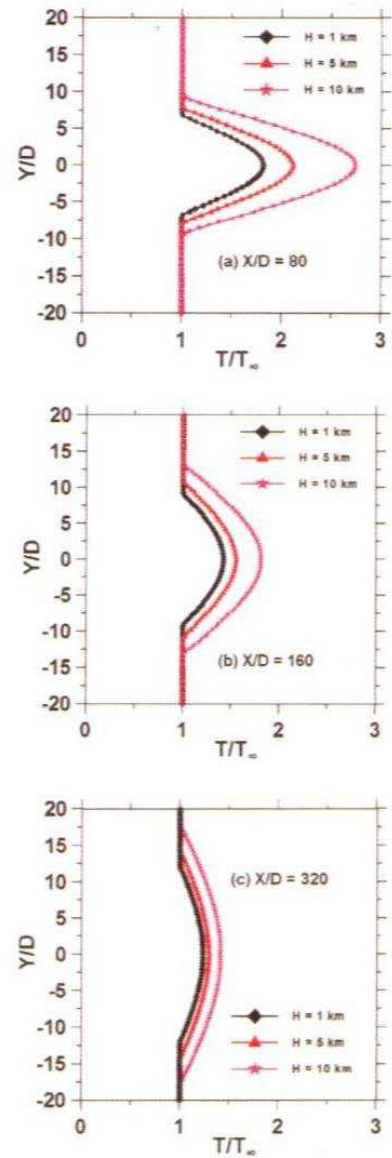


Fig.15 Comparison of Static Temperature Profiles at Different Axial Locations

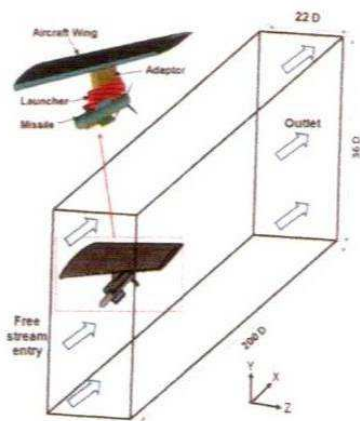


Fig.16 Schematic Picture of Computational Domain in Presence of Aircraft Wing

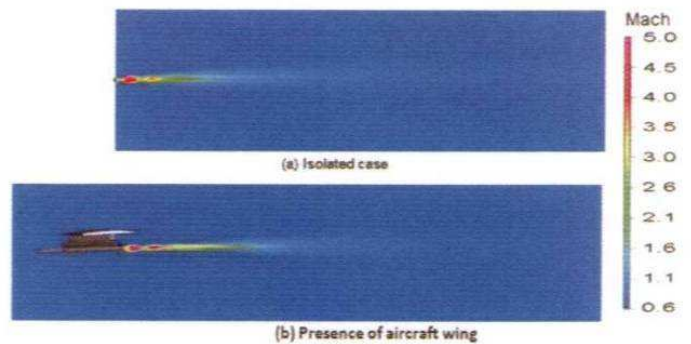


Fig.17 Mach Number Comparison Between Isolated Plume and the Plume in the Presence of Aircraft Wing

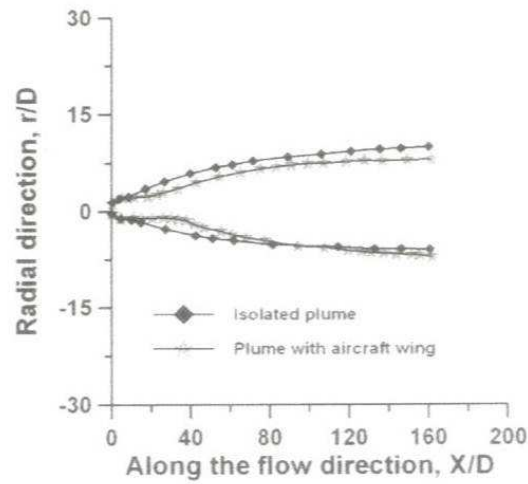


Fig.18 Comparison of Plume Boundaries Between Isolated Plume and the Plume in the Presence of Aircraft Wing

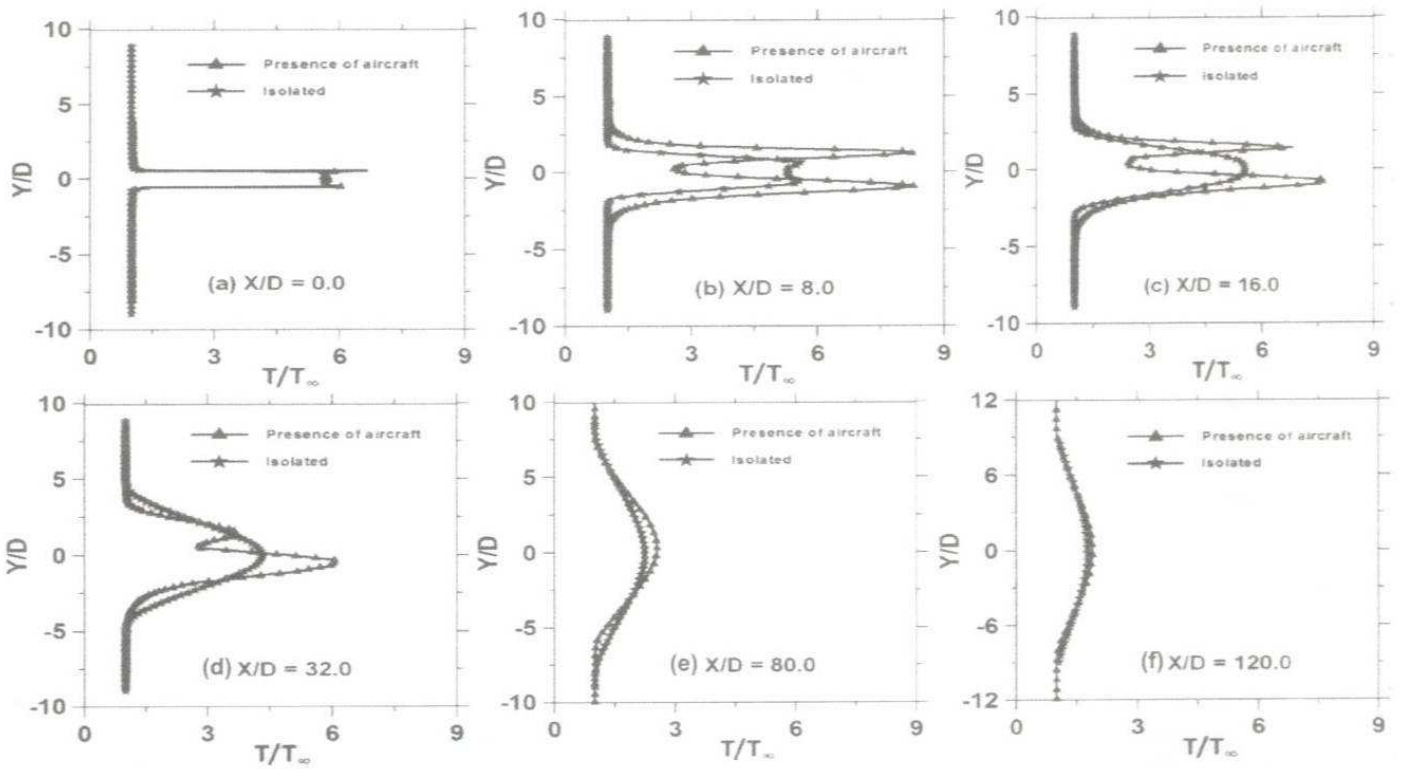


Fig.19 Comparison of Temperature Ratio for with and without Presence of Aircraft Wing